Shape of the hot topological charge density spectral function

Laine, M.

2022-11-21

Laine , M , Niemi , L , Procacci , S & Rummukainen , K 2022 , ' Shape of the hot topological charge density spectral function ' , Journal of High Energy Physics , no. 11 , 126 . https://doi.org/10.1007/JHEP11(20

http://hdl.handle.net/10138/352947
https://doi.org/10.1007/JHEP11(2022)126

JHEP

Published for SISSA by Springer

Received: October 6, 2022
Revised: November 3, 2022
Accepted: November 4, 2022
Published: November 21, 2022

Shape of the hot topological charge density spectral function

M. Laine,[a] **L. Niemi,**[b,c] **S. Procacci**[a] **and K. Rummukainen**[c]

[a] *AEC, Institute for Theoretical Physics, University of Bern, Sidlerstrasse 5, CH-3012 Bern, Switzerland*

[b] *Tsung-Dao Lee Institute, Shanghai Jiao Tong University, Shanghai 200240, China*

[c] *Department of Physics and Helsinki Institute of Physics, P.O. Box 64, FI-00014 University of Helsinki, Finland*

E-mail: laine@itp.unibe.ch, lauri.b.niemi@helsinki.fi, procacci@itp.unibe.ch, kari.rummukainen@helsinki.fi

Abstract: After motivating an interest in the shape of the topological charge density spectral function in hot Yang-Mills theories, we estimate it with the help of thermally averaged classical real-time simulations, for $N_{\rm c} = 2, 3$. After subtracting a perturbative contribution at large frequencies, we observe a non-trivial shape at small frequencies (a dip rather than a peak), interpolating smoothly towards the sphaleron rate at zero frequency. Possible frequency scales making an appearance in this shape are discussed. Implications for warm axion inflation and reheating, and for imaginary-time lattice measurements of the strong sphaleron rate, are recapitulated.

Keywords: Early Universe Particle Physics, Non-Zero Temperature and Density, Cosmology of Theories BSM, Quark-Gluon Plasma

ArXiv ePrint: 2209.13804

https://doi.org/10.1007/JHEP11(2022)126

JHEP11(2022)126

Contents

JHEP11(2022)126

1 Introduction

The operator known as the topological charge density χ (cf. eq. (2.1)) plays a remarkable role in non-Abelian quantum field theory. For the weak gauge group, it is sensitive to processes responsible for anomalous baryon plus lepton number violation [1]. The violation rate is believed to be fast at high temperatures and therefore important for baryogenesis [2], a fact that has led to its detailed numerical determination [3]. On the semiclassical level, the gauge field configurations mediating baryon plus lepton number violation in the Higgs phase are known as sphalerons [4]. Consequently the thermal rate is generically referred to as the sphaleron rate, or the Chern-Simons diffusion rate.

An analogue of the sphaleron rate originating from the strong gauge group may be of interest as well. It affects the evolution of QCD axions [5], among the most studied dark matter candidates. It leads to a fast violation of chirality, which has motivated investigations in the context of heavy ion collision experiments (cf., e.g., ref. [6] for recent work and references). Finally, the topological charge density plays an essential role in models of natural inflation [7–9]. Indeed numerical results for the strong sphaleron rate [10] have found use in that context [11–17], and may induce an efficient reheating mechanism as well [18].

On the technical level, thermal rates are often referred to as transport coefficients. Through so-called Kubo relations, they can be extracted from equilibrium 2-point correlation functions. Specifically, if $C_{\rm S}(\omega)$ denotes a Fourier transform of a 2-point correlator $C_{\rm S}(t)$ with a specific time ordering (cf. eq. (2.3)), then the sphaleron rate is given by $\Gamma_{\rm sph} = \lim_{\omega\to 0} C_{\rm S}(\omega)$ (for a discussion that does not rely on perturbative arguments or physical intuition, see ref. [19]).

The focus of the current investigation is the *shape* of $C_{\rm S}(\omega)$, which contains additional information. The shape is relevant, for example, in theories in which a scalar field φ, notably

an inflaton as mentioned above, couples to a plasma through the operator $\mathcal{L} \supset -\varphi\chi/f_a$. Then it is the ω-dependence that determines the efficiency of the friction that the plasma exerts on φ in different temperature domains [14]. Another example is that estimating the rate of anomalous chirality violation in QCD requires imaginary-time lattice simulations [6], and then it would be important to have an ansatz for the ω-dependence. Even though the QCD coupling is so large that our methods are not reliable on a quantitative level, it is believed that large couplings smoothen spectral functions rather than insert sharp features in them, whereby our results could still be helpful on the qualitative level.

The plan of this paper is the following. After formulating the technical problem (section 2), we review the framework of thermally averaged classical simulations that we use for addressing it (section 3), and describe practical details of the numerical effort (section 4). Subsequently we discuss our slightly unexpected results for the sphaleron rate (section 5). The main part is the analysis of the shape of the spectral function (section 6), after which conclusions and an outlook can be offered (section 7). Details of a perturbative computation are deferred to appendix A.

2 Formulation of the problem

In pure SU($N_{\rm c}$) Yang-Mills theory, the topological charge density is defined as

$$\chi \equiv c_\chi\, \epsilon^{\mu\nu\rho\sigma} g^2 F^a_{\mu\nu} F^a_{\rho\sigma}\,, \quad a \in \{1,\ldots,N_{\rm c}^2-1\}\,, \quad c_\chi \equiv \frac{1}{64\pi^2}\,, \tag{2.1}$$

where $T^a F^a_{\mu\nu} = [D_\mu, D_\nu]/(ig)$ is the Yang-Mills field strength; $D_\mu \equiv \partial_\mu + igT^a A^a_\mu$ is a covariant derivative; $g^2 \equiv 4\pi\alpha$ is the Yang-Mills coupling; and T^a are Hermitean generators of SU($N_{\rm c}$), normalized as $\mathrm{Tr}\,[T^a T^b] = \delta^{ab}/2$. The topological charge density is a peculiar quantity, in that for smooth gauge configurations it is a total derivative, evaluating to an integer after integration over spacetime. In quantum field theory, it is simply a local pseudoscalar operator, which displays non-trivial correlation functions at all time and distance scales.

In this study we are interested in real-time correlation functions of the spatial average of χ, in thermal equilibrium at a temperature T. Different time orderings yield different real-time correlation functions. Theoretical discussions (and also the title of this paper) often refer to a spectral function, which is defined as

$$\rho(\omega) \equiv \int_{-\infty}^{\infty} \mathrm{d}t\, e^{i\omega t} \int_{\mathbf{x}} \Big\langle \frac{1}{2}\big[\chi(t,\mathbf{x})\,,\,\chi(0,\mathbf{y})\big] \Big\rangle\,. \tag{2.2}$$

The spectral function can alternatively be viewed as the imaginary part of a retarded correlator, $\rho(\omega) = \mathrm{Im}\, C_{\rm R}(\omega + i0^+)$. However, as discussed in section 1, physical observables are more directly related to a "statistical", or time-symmetric 2-point correlator of χ,

$$C_{\rm S}(t) \equiv \int_{\mathbf{x}} \Big\langle \frac{1}{2}\{\chi(t,\mathbf{x})\,,\,\chi(0,\mathbf{y})\} \Big\rangle\,, \quad C_{\rm S}(\omega) \equiv \int_{-\infty}^{\infty} \mathrm{d}t\, e^{i\omega t}\, C_{\rm S}(t)\,. \tag{2.3}$$

Given that $C_{\rm S}(-t) = C_{\rm S}(t)$, the Fourier transform can equivalently be expressed as

$$C_{\rm S}(\omega) = 2\int_0^{\infty} \mathrm{d}t\, \cos(\omega t)\, C_{\rm S}(t)\,. \tag{2.4}$$

JHEP11(2022)126

A text-book proof, obtained by inserting complete sets of energy eigenstates in the thermal expectation values, shows that the spectral and statistical correlators are related by

$$C_{\rm S}(\omega) = \left[1 + 2n_{\rm B}(\omega)\right] \rho(\omega)\,, \tag{2.5}$$

where $n_{\rm B}(\omega) \equiv 1/(e^{\beta\omega} - 1)$ is the Bose distribution, with $\beta \equiv 1/T$. In the domain that we are interested in, viz. $\omega \ll T$, the spectral function can thus be obtained from the statistical correlator as

$$\rho(\omega) \quad \overset{|\omega| \ll T}{=} \quad \frac{\omega\, C_{\rm S}(\omega)}{2T}\,. \tag{2.6}$$

Now, the appearance of an anticommutator in eq. (2.3) guarantees that $C_{\rm S}(\omega)$ has formally a classical limit,

$$C_{\rm S}^{\rm (cl)}(\omega) \equiv \lim_{\hbar \to 0} C_{\rm S}(\omega)\,. \tag{2.7}$$

It turns out that in an interacting theory, the classical limit is singular [20], as classical field theory is plagued by Rayleigh-Jeans type of ultraviolet (UV) divergences. However, if we keep the UV cutoff finite, by introducing a *spatial* lattice discretization, then the classical limit exists. It is believed that studies with such a framework can reveal the magnitude of the transport coefficient $\lim_{\omega\to 0} C_{\rm S}(\omega)$ at weak coupling, $\alpha N_{\rm c} \ll 1$ [21–23]. The premise of the present investigation is that it should also be possible to use classical lattice gauge theory to estimate the shape of $C_{\rm S}(\omega)$, as long as we are in the Bose-enhanced domain $|\omega| \ll T$.

The UV divergences mentioned above distort physics at the frequency scale of the cutoff, $\omega \sim 1/a$. In order to alleviate this, we compute $C_{\rm S}^{\rm (cl)}(\omega)$ in leading-order perturbation theory for $\omega \sim 1/a$, where a is the lattice spacing. In this UV regime, classical lattice gauge theory is weakly coupled. The perturbative result can be subtracted from the lattice measurement,[1] whose goal is to estimate $C_{\rm S}^{\rm (cl)}(\omega)$ non-perturbatively at $\omega \sim \{\alpha^2 N_{\rm c}^2 T^2 a, \alpha N_{\rm c} T\}$. The first scale replaces the physical infrared (IR) scale $\sim \alpha^2 N_{\rm c}^2 T$ in classical lattice gauge theory [24]. The second scale represents the colour-magnetic screening scale, but it can also affect real-time phenomena, given that space-like separated real-time fluctuations can to a good approximation be treated as equal-time ones. With a suitable re-interpretation of these IR frequency scales, the results then arguably apply, on a qualitative level, to the continuum problem as well [24, 25] (cf. sections 6 and 7).[2]

3 Definition of classical lattice gauge theory

We consider a theory discretized in spatial directions and with a continuous time coordinate [31, 32]. Quantizing this theory in the gauge $A_0^a = 0$ and then taking the classical

[1] The perturbative expression vanishes as $\omega \to 0$ and therefore plays no role in the estimation of the transport coefficient $\lim_{\omega\to 0} C_{\rm S}(\omega)$.

[2] In recent numerical determinations of the sphaleron rate, a different logic is followed (cf., e.g., refs. [3, 10] and references therein). By integrating out the scale $\sim gT$, it is possible to derive a simplified Langevin description for the IR dynamics [26, 27]. A great advantage of this setup is that it is UV-finite [28, 29]. However, there are drawbacks, namely that the simplest form of the theory, used for numerical simulations [3, 10], applies only to the smallest frequencies, whereas we would like to resolve the shape up to somewhat larger frequencies; and that it involves an expansion not only in g, but also in $1/\ln(1/g)$ [30].

JHEP11(2022)126

limit, yields the partition function (cf., e.g., ref. [25] and references therein)

$$Z^{(\mathrm{cl})} = \int \mathcal{D}U_i \, \mathcal{D}\mathcal{E}_i \, \delta(G) \exp\biggl\{ -\frac{1}{g^2 T a} \sum_{\mathbf{x}} \biggl[\sum_{i,j} \mathrm{Tr}\, \Bigl(\mathbb{1} - P_{ij} \Bigr) + \sum_i \mathrm{Tr}\, \Bigl(\mathcal{E}_i^2 \Bigr) \biggr] \biggr\} \,, \tag{3.1}$$

where U_i are link matrices; $\mathcal{E}_i$ the corresponding canonical momenta; $P_{ij}(\mathbf{x}) = U_i(\mathbf{x}) U_j(\mathbf{x} + a\mathbf{i}) U_i^\dagger(\mathbf{x} + a\mathbf{j}) U_j^\dagger(\mathbf{x})$ is a plaquette;

$$G(\mathbf{x}) \equiv \sum_i \Bigl[\mathcal{E}_i(\mathbf{x}) - U_i^\dagger(\mathbf{x} - a\mathbf{i}) \mathcal{E}_i(\mathbf{x} - a\mathbf{i}) U_i(\mathbf{x} - a\mathbf{i}) \Bigr] \tag{3.2}$$

are Gauss law operators, set to zero at every location $\mathbf{x}$ by the constraints in eq. (3.1); and $\mathbf{i}$ is a unit vector in the i-direction. The equations of motion read

$$a\, \partial_t U_i(x) = i \mathcal{E}_i(x) U_i(x) \,, \tag{3.3}$$

$$a\, \partial_t \mathcal{E}_i^b(x) = 2 \sum_{j \neq i} \mathrm{Im}\, \mathrm{Tr}\, \Bigl\{ T^b \Bigl[P_{ji}(x) + P_{-ji}(x) \Bigr] \Bigr\} \,, \tag{3.4}$$

where $U_{-j}(x) \equiv U_j^\dagger(x - a\mathbf{j})$, and $x \equiv (t, \mathbf{x})$. The Gauss law at each position $\mathbf{x}$, and the Hamiltonian, are constants of motion. For later reference we also note that $\mathcal{E}_i$ is related to a continuum electric field E_i as $\mathcal{E}_i = a^2 g E_i$, implying that the Hamiltonian (appearing as $e^{-H/T}$) contains

$$H \supset \frac{1}{g^2 a} \sum_{\mathbf{x}} \sum_i \mathrm{Tr}\, \Bigl(\mathcal{E}_i^2 \Bigr) = \sum_{\mathbf{x}} a^3 \sum_i \mathrm{Tr}\, \Bigl(E_i^2 \Bigr) \,. \tag{3.5}$$

Now, the continuum operator from eq. (2.1) can be written as

$$\chi = 4 c_\chi \, \epsilon_{ijk} \, g^2 F_{0i}^b F_{jk}^b = 4 c_\chi \, \epsilon_{ijk} \, g^2 E_i^b F_{jk}^b = -8 i c_\chi \, \epsilon_{ijk} \, \mathrm{Tr}\, \bigl(g E_i \, i g F_{jk} \bigr) \,. \tag{3.6}$$

The electric part could be expressed in terms of $\mathcal{E}_i$, but for practical measurements it turns out to be important to symmetrize the discretization (cf., e.g., ref. [33]). According to eq. (3.3), the electric fields $\mathcal{E}_i(x)$ affect the evolution of the links placed between x and $x + a\mathbf{i}$. We can thus imagine that electric fields "live" at $x + \frac{a\mathbf{i}}{2}$. For the position x it is best to associate an electric field covariantly averaged from $x + \frac{a\mathbf{i}}{2}$ and $x - \frac{a\mathbf{i}}{2}$,

$$\overline{\mathcal{E}}_i(x) \equiv \frac{1}{2} \Bigl[\mathcal{E}_i(x) + U_i^\dagger(x - a\mathbf{i}) \mathcal{E}_i(x - a\mathbf{i}) U_i(x - a\mathbf{i}) \Bigr] \,. \tag{3.7}$$

The parts appearing here are the same as needed in the Gauss law, cf. eq. (3.2), now just averaged over, rather than subtracted from each other.

As far as the magnetic field goes, it is discretized by making use of a "clover",

$$i g F_{jk}(x) \equiv \frac{Q_{jk}(x) - Q_{kj}(x)}{8 a^2} \,, \tag{3.8}$$

$$Q_{jk}(x) \equiv P_{jk}(x) + P_{k-j}(x) + P_{-j-k}(x) + P_{-kj}(x) \,. \tag{3.9}$$

JHEP11(2022)126

Making use of translational invariance, the measurement of eq. (2.3) therefore originates from

$$a^5 C_{\rm S}^{\rm (cl)}(t) \equiv \frac{1}{N_s^3} \sum_{\mathbf{x},\mathbf{y}} \Big\langle a^4 \chi^{\rm (cl)}(t,\mathbf{x})\, a^4 \chi^{\rm (cl)}(0,\mathbf{y}) \Big\rangle \,, \tag{3.10}$$

$$a^4 \chi^{\rm (cl)} \equiv -2i c_\chi\, \epsilon_{ijk}\, {\rm Tr}\, \Big(\overline{\mathcal{E}}_i\, Q_{jk} \Big) \,. \tag{3.11}$$

On the right-hand side of eq. (3.10), factors of a from the inverse volume and two summation measures have been combined as $a^{-3}(a^3)^2 a^5 = (a^4)^2$; N_s is the number of lattice points in spatial directions; the time dependence is obtained by solving the equations of motion in eqs. (3.3) and (3.4); and initial conditions are generated according to the weight in eq. (3.1).

We note that, unlike in continuum, eq. (3.11) is not "topological", i.e. a total derivative (or a difference). Much has been said about this in the literature, but we are not worried, as the operator still has the correct IR properties at small energies and momenta, and computable UV properties at energy scales $\sim 1/a$. More comments on this are offered in section 5.

Once we have measured $C_{\rm S}^{\rm (cl)}(t)$ from eq. (3.10) and taken a Fourier transform according to eq. (2.4), the results are conveniently normalized as [10, 25]

$$\frac{C_{\rm S}^{\rm (cl)}(\omega)}{(\alpha T)^4} = \frac{a^4 C_{\rm S}^{\rm (cl)}(\omega)}{16\, c_\chi^2\, (a g^2 T)^4} \,. \tag{3.12}$$

4 Simulations and measurements

For practical measurements, the setup outlined above needs to be made concrete through a number of further ingredients: the time evolution needs to be discretized, a correctly thermalized ensemble of initial configurations needs to be generated, observables need be averaged as much as possible to reduce noise, the spatial volume needs to be made large enough so that it has no practical effect, and the equations of motion need to be solved for a long enough time that small frequencies can be addressed (including $\omega \to 0$ as needed for $\Gamma_{\rm sph}$, cf. eq. (5.1)). In this section we describe how these challenges can be overcome.

Time discretization. For representing the time evolution in eqs. (3.3) and (3.4), we choose a temporal lattice spacing $a_t \ll a$. In practice, after tests, we settled on $a_t = 0.02a$, which turns out to yield sufficient accuracy at a manageable cost.

Even if the links and electric fields are placed at the same time in the operator $\chi^{\rm (cl)}$ in eq. (3.11), for a numerical evaluation it is helpful to first evolve the links by $a_t/2$ in the time direction. Subsequently, we leap-frog the evolutions of the links and the electric fields,

$$U_i\Big(x + \frac{a_t \mathbf{0}}{2}\Big) \equiv \exp\Big[i \frac{a_t}{a}\, \overline{\mathcal{E}}_i(x) \Big] U_i\Big(x - \frac{a_t \mathbf{0}}{2}\Big) \,, \tag{4.1}$$

$$\mathcal{E}_i^b(x + a_t\mathbf{0}) = \mathcal{E}_i^b(x) + \frac{2a_t}{a} \sum_{j\neq i} {\rm Im\, Tr} \Big\{ T^b \Big[P_{ji}\Big(x + \frac{a_t\mathbf{0}}{2}\Big) + P_{-ji}\Big(x + \frac{a_t\mathbf{0}}{2}\Big) \Big] \Big\} \,, \tag{4.2}$$

where $\mathbf{0}$ is a unit vector in the time direction. For measuring $\chi^{\rm (cl)}$, the Hamiltonian, or for checking the conservation of the Gauss law constraints, the links and electric fields are brought back to the same time, by performing an additional half-step update of U_i.

JHEP11(2022)126

It is important to stress that the Hamiltonian and the Gauss law constraints are conserved for $a_t \ll a$ and in practice stay unchanged within our numerical resolution. Therefore, any configuration obtained after real-time evolution is an equally valid representative of the thermal ensemble. In other words, the system is time-translation invariant.

Thermalization. The generation of a thermal ensemble representing eq. (3.1) differs from a standard lattice simulation by the need to satisfy the Gauss constraint at each position. To implement this, we have followed the procedure described in ref. [34], which is summarized here. One full thermalization "sweep" (over the spatial lattice) consists of the following steps:

(i) We first pull $\{\mathcal{E}_i(\mathbf{x})\}$ from a Gaussian distribution according to the last term in eq. (3.1), leaving the links $\{U_i(\mathbf{x})\}$ untouched.

(ii) The Gauss law constraints $G(\mathbf{x}) = 0$ are subsequently enforced by repeatedly modifying

$$\mathcal{E}_i(\mathbf{x}) \to \mathcal{E}_i(\mathbf{x}) - \gamma \left[G(\mathbf{x}) - U_i(\mathbf{x}) G(\mathbf{x} + a\mathbf{i}) U_i^\dagger(\mathbf{x}) \right] , \quad \gamma > 0 , \tag{4.3}$$

with the $G(\mathbf{x})$ recalculated at each step. This corresponds to a gradient flow minimization of an auxiliary Hamiltonian $\sum_{\mathbf{x}} G^a(\mathbf{x}) G^a(\mathbf{x})$ [22]. Following ref. [34], the update size γ is alternated between 5/48 and 5/24, and the process is repeated until the average per site violation $\sum_{\mathbf{x}} G^a(\mathbf{x}) G^a(\mathbf{x}) / N_s^3$ is smaller than 10^{-12}.

(iii) Steps (i) and (ii) give a duly thermalized configuration $\{\mathcal{E}_i(\mathbf{x})\}$ for fixed $\{U_i(\mathbf{x})\}$. In order to generate new links, we allow energy to redistribute between the $\{\mathcal{E}_i(\mathbf{x})\}$ and $\{U_i(\mathbf{x})\}$, by evolving the system with eqs. (4.1) and (4.2), until time $t = a$. As mentioned above, the Gauss law constraints remain satisfied in this evolution.

Our simulations are initiated by performing 500 such thermalization sweeps on a cold configuration. In the physical measurement runs, called time trajectories, the time evolution according to eqs. (4.1) and (4.2) is continued for a longer time than in a sweep, typically $t_{\max} = (10 - 100)a$. The separate time trajectories, of which there are $\sim 10^4 - 10^5$ (cf. tables 1 and 2), are separated by 20 additional sweeps, in order to reduce autocorrelations.

Averaging and error analysis. The time coordinate t appearing in the measurement of eq. (3.10) is really a time difference. Given the time-translation invariance of our system, this implies that a single trajectory permits for many measurements, by considering all time pairings. If the m^{th} trajectory is sampled at times $t_n = n a_t$, with $n = 0, \ldots, N-1$, where $(N-1)a_t = t_{\max}$ sets the maximal time, and the average topological charge density is denoted by $\bar{\chi}_n^{(m)} \equiv \frac{1}{N_s^3} \sum_{\mathbf{x}} \chi^{(\text{cl})}(t_n, \mathbf{x})$, then the measurement of eq. (3.10) can be implemented as

$$a^5 C_{\text{S}}^{(\text{cl})}(t_j) = \lim_{M \to \infty} \frac{N_s^3}{M} \sum_{m=1}^{M} \frac{1}{N-j} \sum_{n=0}^{N-j-1} \left(a^4 \bar{\chi}_{n+j}^{(m)} \right) \left(a^4 \bar{\chi}_n^{(m)} \right) , \tag{4.4}$$

where M is the number of trajectories. The normalization by $1/(N-j)$ accounts for the fact that a single trajectory gives multiple measurements.

JHEP11(2022)126

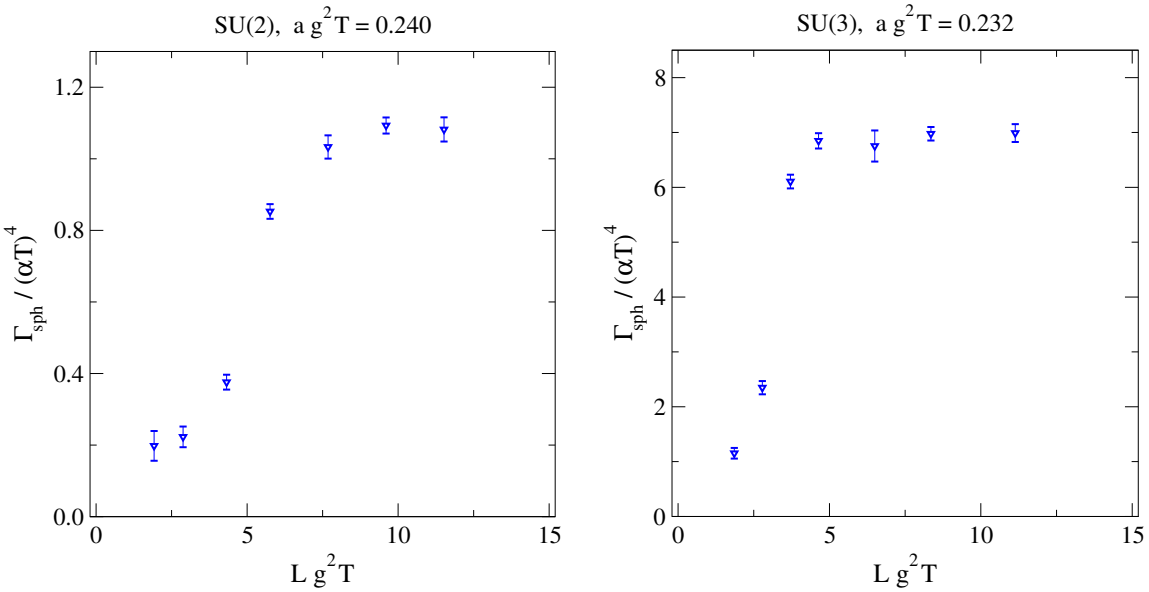

Figure 1. Demonstration of the dependence of $\Gamma_{\rm sph}$ from eq. (5.1) on the spatial extent $L = aN_s$ of the box. As expected theoretically [36], the volume dependence is exponentially small when L is large compared with the colour-magnetic screening scale $\sim 1/(g^2T)$. For SU(3), smaller volumes suffice in these units, as thermal glueball masses increase in proportion to $N_{\rm c}$.

In practice, the number of trajectories is finite, and then the limit in eq. (4.4) cannot be taken. This implies that the measurement has statistical errors. We estimate them with the jackknife method, by dividing the total ensemble of trajectories into ten separate blocks, and applying the jackknife procedure to the blocked measurements.

Given $a^5 C_{\rm S}^{\rm (cl)}(t_j)$ from eq. (4.4), the Fourier transform from eq. (2.4) is taken with Simpson's rule. The trapezoidal approximation would yield

$$a^4 C_{\rm S}^{\rm (cl)}(\omega) \simeq 2 \sum_{j=0}^{\infty} \frac{a_t}{a} \cos(\omega t_j)\, a^5 C_{\rm S}^{\rm (cl)}(t_j) \left(1 - \frac{\delta_{j,0}}{2}\right), \tag{4.5}$$

however given the large amount of data, we have taken measurements only at every 5th time step, and therefore employ a higher-order scheme. Specifically, given that the equal-time value $t_j = 0$ plays an important role in the Fourier transform, we have implemented a custom routine for the first time step, using the knowledge that $C_{\rm S}^{\rm (cl)}(t)$ is a symmetric function of t. The subsequent intervals have been treated with quadratic discretization.

Finite spatial volume. Any simulation takes place in a finite periodic box, $V = L^3$, $L \equiv aN_s$. Given that non-Abelian thermal field theory has a mass gap, with the corresponding confinement scale given by $\sim g^2T$ [35], finite-volume effects are exponentially small if $L\, g^2T \gg 1$ [36]. However, we need to carry out practical tests to see the numerical coefficient on the right-hand side of this inequality, so that finite-volume effects are indeed smaller than statistical errors.

In figure 1, values of $\Gamma_{\rm sph}$ obtained from eq. (5.1) are shown for a number of box sizes, both for $N_{\rm c} = 2$ and $N_{\rm c} = 3$. For small box sizes, the sphaleron rate is reduced (even if with

JHEP11(2022)126

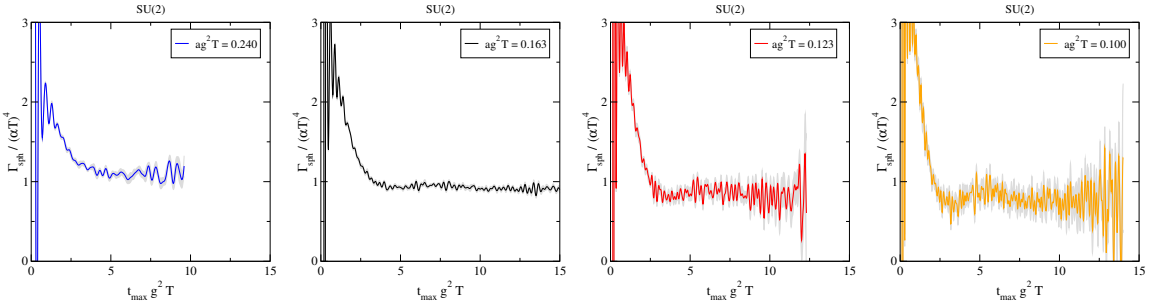

Figure 2. Demonstration of the dependence of $\Gamma_{\rm sph}$ from eq. (5.1) on the time extent $t_{\rm max}$. Similarly to the volume dependence in figure 1, the dependence on $t_{\rm max}$ gets stabilized when $t_{\rm max}$ is large compared with the colour-magnetic scale $\sim 1/(g^2T)$, apart from fast oscillations that average to zero.

our local definition it does not go to zero). As the volume is increased, the rate saturates. For SU(2) this happens when $Lg^2T \geq 8.0$, for SU(3) when $Lg^2T \geq 5.0$. The box sizes for our production runs, listed in tables 1 and 2, have been chosen so that these inequalities are comfortably satisfied.

Finite time extent. Another important extent is that of the real-time interval, which we denote by $t_{\rm max}$. There is less theoretical intuition about $t_{\rm max}$ than L, but practical tests are easier to carry out, as $t_{\rm max}$ can be varied within a single simulation.

Examples of sphaleron rates with varying $t_{\rm max}$ are shown in figure 2. Remarkably, we observe a partly similar behaviour as for finite-volume effects in figure 1, namely a saturation as a certain value of $t_{\rm max}\, g^2T$ is exceeded, which is however now overlayed with rapid oscillations.

Considering first the saturation point, it decreases slightly with decreasing ag^2T. If we associate the inverse of the saturation point with a frequency scale, we can then say that there is a frequency scale which increases with decreasing ag^2T. Frequency scales could be interpreted as threshold energies needed to excite a number of glueballs.[3] The odd discrete quantum numbers of χ suggest that the glueball ensemble should be odd under the same inversions, and that it therefore corresponds to a non-perturbative Debye mass [37]. A constituent Debye mass indeed diverges in classical lattice gauge theory, cf. eq. (6.8). A divergence also appears in the height of a plateau in $C_{\rm S}^{\rm (cl)}(\omega)$, cf. figure 5. These observations may provide a rough explanation for the movement of the saturation point as seen in figure 2.

Turning to the oscillations, we note that they could be interpreted as a mild "sign problem", i.e. cancellation between positive and negative values when integrating over $C_{\rm S}^{\rm (cl)}(t)$ in order to determine $\lim_{\omega\to 0} C_{\rm S}^{\rm (cl)}(\omega)$, cf. eq. (4.5). In order to deal with this, we have adopted a recipe whereby our measurement of $\Gamma_{\rm sph}$ does not originate from a single fixed $t_{\rm max}$, but rather measurements in the range $t_{\rm max}\, g^2T \in (\bar\theta \pm \Delta\theta)$. Within the width $\Delta\theta = 1.0\ (0.5)$ for $N_{\rm c} = 2\ (3)$, measurements have been combined as statistical scatter,[4]

[3] In this language, spectral weight at very small ω does not correspond to exciting a number of glueballs, but rather to scattering off them.

[4] This is supported by the observation that if the noise were uncorrelated and the same number of measurements were carried out at each $t_{\rm max}$, the overall noise magnitude in figure 2 should scale as $\sim \sqrt{t_{\rm max}}$. At moderate times, a gradual increase can indeed be discerned.

JHEP11(2022)126

$N_{\rm c} = 2$

$\beta_{\rm L}$	$a_{\rm bare}\, g^2 T$	N_s	$L\, g^2 T$	$t_{\rm max}\, g^2 T$	# traj.	$\Gamma_{\rm sph}/(\alpha T)^4$	$\Gamma^{\rm cooled}_{\rm sph[25]}/(\alpha T)^4$
4.63...	0.863	10	8.63	≤ 9.49	50000	$0.885(0.010)_{\rm syst}(0.008)_{\rm stat}$	3.82(0.14)
6.60...	0.606	16	9.70	≤ 9.09	100000	$1.061(0.008)_{\rm syst}(0.011)_{\rm stat}$	2.69(0.08)
8.64...	0.463	20	9.26	≤ 9.26	57205	$1.129(0.010)_{\rm syst}(0.013)_{\rm stat}$	2.28(0.04)
12.7...	0.314	32	10.0	≤ 12.6	50000	$1.128(0.025)_{\rm syst}(0.011)_{\rm stat}$	1.64(0.04)
13.5...	0.295	—	—	—	—	—	1.53(0.04)
16.6...	0.240	40	9.60	≤ 9.60	46580	$1.093(0.008)_{\rm syst}(0.021)_{\rm stat}$	1.31(0.05)
24.5...	0.163	60	9.78	≤ 26.1	78470	$0.944(0.012)_{\rm syst}(0.004)_{\rm stat}$	0.95(0.03)
32.5...	0.123	80	9.84	≤ 12.3	59652	$0.870(0.023)_{\rm syst}(0.012)_{\rm stat}$	0.68(0.03)
40.0...	0.100	96	9.60	≤ 14.0	41132	$0.816(0.059)_{\rm syst}(0.010)_{\rm stat}$	—
53.3...	0.075	128	9.60	≤ 12.0	33373	$0.742(0.112)_{\rm syst}(0.015)_{\rm stat}$	—

Table 1. Our results for the sphaleron rate for $N_{\rm c} = 2$, compared with "cooled" rates from table 2 of ref. [25], however we have undone the improvement employed in the latter study, by making use of eq. (5.2). The values of $a_{\rm bare}\, g^2 T$ are treated as "exact", whereas digits have been truncated from the values of $\beta_{\rm L}$ shown (cf. eq. (5.3)). These results are illustrated in figure 3.

whereas the variation $\bar{\theta} = 5 - 8$ $(4 - 6)$ for $N_{\rm c} = 2$ (3) has been employed for estimating the systematic uncertainty of this procedure. The final statistical error is the average of the jackknife errors from all values of $\bar{\theta}$ considered. In tables 1 and 2, the systematic and statistical uncertainties are displayed separately, whereas in figure 3, they have been combined in quadrature.

Finally, we note that a finite value of $t_{\rm max}$ implies that we have a limited resolution in ω. Recalling the symmetry of $C_{\rm S}^{\rm (cl)}(t)$ under $t \to -t$, independent frequencies should be chosen as multiples of $\pi/t_{\rm max}$.

5 Fresh look at the sphaleron rate

Having established the technical setup, we proceed to the results, considering first the sphaleron rate,

$$\Gamma_{\rm sph} = \lim_{\omega \to 0} C_{\rm S}(\omega)\,. \tag{5.1}$$

The sphaleron rate has previously been measured with Hamiltonian simulations in refs. [10, 25], however with a different definition. While the simulation itself proceeded in the same way, for measurements the gauge configurations were "cooled" towards the solution of classical equations of motion, removing short-distance fluctuations and arguably turning χ into a topological observable.[5] Subsequently, $\Gamma^{\rm cooled}_{\rm sph}$ was extracted as a diffusion coefficient related to the movement of the cooled Chern-Simons number. We note that even though physically intuitive, such a definition does not lend itself to an operator definition that emerges naturally from quantum field theory; a cooled spectral function is not the same

[5] Cooling in those studies amounts to the introduction of a fictitious coordinate η and the solution of equations of the type $\partial_\eta \Phi = -\delta S_{\rm E}/\delta\Phi$, where $S_{\rm E}$ denotes the (3-dimensional) Euclidean action and Φ the ensemble of fields. The initial condition $\Phi(\eta \to 0^+)$ is taken from the Monte Carlo history, whereas the asymptotic value $\Phi(\eta \to \infty)$ satisfies $\delta S_{\rm E}/\delta\Phi = 0$ and is thus a solution of equations of motion.

JHEP11(2022)126

$N_{\rm c} = 3$

$\beta_{\rm L}$	$a_{\rm bare}\, g^2T$	N_s	$L\, g^2T$	$t_{\rm max}\, g^2T$	# traj.	$\Gamma_{\rm sph}/(\alpha T)^4$	$\Gamma^{\rm cooled}_{\rm sph[10]}/(\alpha T)^4$
9.35...	0.642	20	12.8	≤ 10.0	78775	$5.054(0.037)_{\rm syst}(0.024)_{\rm stat}$	41.6(0.7)
10.8...	0.553	20	11.1	≤ 10.1	41738	$5.575(0.038)_{\rm syst}(0.040)_{\rm stat}$	29.6(0.4)
12.3...	0.488	20	9.76	≤ 10.2	32207	$6.101(0.061)_{\rm syst}(0.055)_{\rm stat}$	24.1(0.5)
13.8...	0.433	20	8.66	≤ 10.0	59666	$6.434(0.011)_{\rm syst}(0.045)_{\rm stat}$	20.3(0.5)
16.8...	0.356	20	7.12	≤ 10.0	54168	$6.764(0.022)_{\rm syst}(0.025)_{\rm stat}$	16.5(0.3)
19.8...	0.302	20	6.04	≤ 10.3	58157	$6.917(0.037)_{\rm syst}(0.058)_{\rm stat}$	13.6(0.3)
25.8...	0.232	36	8.35	≤ 8.12	48400	$6.977(0.084)_{\rm syst}(0.090)_{\rm stat}$	11.4(0.2)
31.9...	0.188	40	7.52	≤ 8.46	63657	$6.641(0.026)_{\rm syst}(0.069)_{\rm stat}$	9.9(0.3)
48.0...	0.125	60	7.50	≤ 8.75	55072	$5.780(0.158)_{\rm syst}(0.086)_{\rm stat}$	—
60.0...	0.100	80	8.00	≤ 8.00	48968	$5.300(0.227)_{\rm syst}(0.086)_{\rm stat}$	—
80.0...	0.075	96	7.20	≤ 8.25	35815	$4.903(0.393)_{\rm syst}(0.130)_{\rm stat}$	—

Table 2. Like table 1 but for $N_{\rm c} = 3$. In this case the cooled rates originate from table 3 of ref. [10], after undoing the improvement employed in that study.

object that affects, e.g., the motion of an axion field coupled to a local pseudoscalar operator. In other words, cooling changes the *expectation value* of $\Gamma_{\rm sph}$, not only its variance.

Another feature in refs. [10, 25] is $\mathcal{O}(a)$ improvement of the parameters used. The idea is that the coefficient in front of the Hamiltonian in eq. (3.1) is replaced through [10]

$$\frac{1}{ag^2T} \;\longrightarrow\; \frac{1}{a_{\rm bare}\, g^2T} \equiv \frac{1}{a_{\rm impr}\, g^2T} + N_{\rm c}\left(0.12084 - \frac{1}{6N_{\rm c}^2}\right). \tag{5.2}$$

The lattice spacing is conventionally reparametrized as

$$\beta_{\rm L} \equiv \frac{2N_{\rm c}}{a_{\rm bare}\, g^2T}\,. \tag{5.3}$$

For us improvement is unnecessary and complicates the discussion, whence we re-tabulate the results from refs. [10, 25] in the last columns of tables 1 and 2 without it. In our notation,

$$ag^2T \equiv a_{\rm bare}\, g^2T\,. \tag{5.4}$$

Our results for $\Gamma_{\rm sph}$ are listed in tables 1 and 2, and shown in figure 3. The pattern observed is simple to state: at coarse lattices, $ag^2T \gg 0.2$, our results are clearly below the cooled ones. In contrast, as we go to $ag^2T \ll 0.2$, two things happen simultaneously:

(i) Our results for $\Gamma_{\rm sph}$ are of the same order of magnitude as $\Gamma^{\rm cooled}_{\rm sph}$. The reason should be that in this regime a scale hierarchy sets in, and the universal IR dynamics responsible for the sphaleron rate takes over from non-universal UV fluctuations. The results are not exactly the same, however. This need not be surprising, as the IR and UV fluctuations do not decouple from each other in a non-renormalizable theory, and as it is difficult to specify which precise UV fluctuations have been removed by the cooling.

(ii) The sphaleron rate $\Gamma_{\rm sph}$ displays approximately linear scaling with ag^2T, as expected from eq. (6.9). This is a key feature of the universal IR dynamics. It has, however,

JHEP11(2022)126

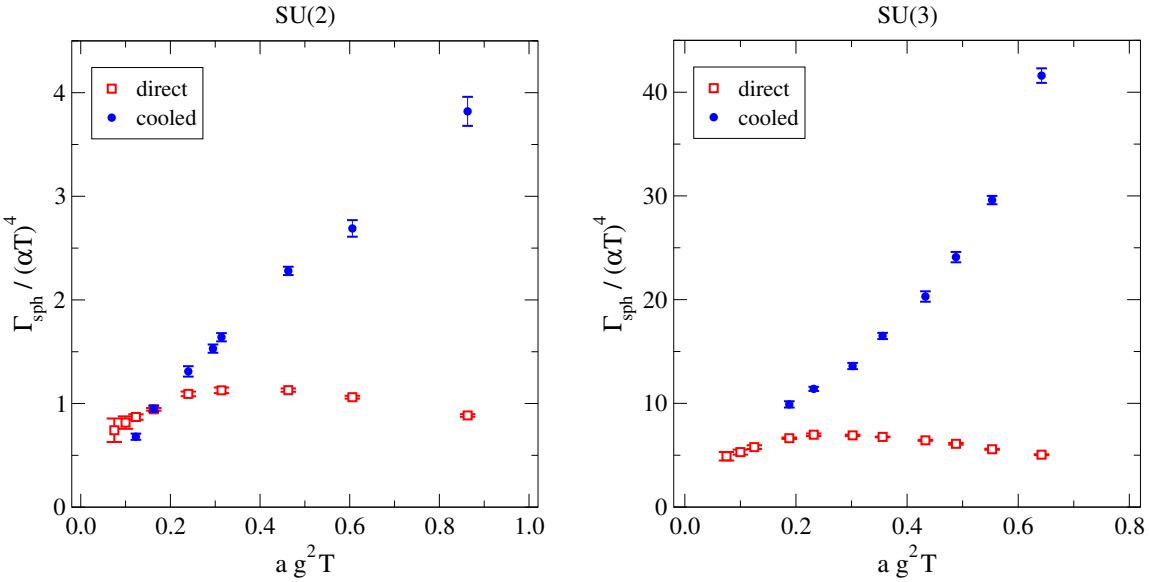

Figure 3. Comparison of our $\Gamma_{\rm sph}$ from eq. (5.1) ("direct") against literature results employing a different definition ("cooled") [10, 25]. The data are as given in tables 1 and 2, with errors combined in quadrature. The results do not agree quantitatively, but both approach zero in the scaling regime $ag^2T \ll 0.2$, with an approximately linear slope, modified by a complicated logarithmic dependence.

been modified by a complicated (unknown but likely non-polynomial) logarithmic dependence, originating from the non-decoupling of the IR and UV fluctuations.

We refer to the regime $ag^2T \ll 0.2$, in which these observations apply, as the *scaling regime*. It is only in the scaling regime that classical lattice gauge theory can be employed for extracting physical information, and therefore we focus on it in the following.

6 Estimate of the shape of the spectral function

We finally turn to the ω-dependence of $C_{\rm S}^{\rm (cl)}(\omega)$. In figure 4, results normalized according to eq. (3.12) are plotted at a few small lattice spacings, where we are in the scaling regime. The results are compared with a leading-order perturbative evaluation, detailed in appendix A. For a better resolution, these results are replotted in figure 5, after the subtraction of the perturbative part and a conversion of the frequency scale into units of g^2T.

The results in figure 5 represent an IR contribution, whose shape we would like to understand. Generalizing on ref. [14], the IR part may be parametrized as

$$\Delta\rho(\omega)\big|_{\rm cont} \equiv \rho(\omega)\big|_{\rm cont} - \rho_{\rm UV}(\omega)\big|_{\rm cont} \tag{6.1}$$

$$\overset{|\omega|\ll gT}{\simeq} \omega\Upsilon_{\rm IR}\mathcal{F}\left(\frac{\omega^2}{\omega_{\rm IR}^2},\frac{\omega^2}{\omega_{\rm M}^2},\ldots\right), \tag{6.2}$$

$$\Upsilon_{\rm IR}\big|_{\rm cont} \equiv \kappa\,\alpha^5 N_{\rm c}^3\left(N_{\rm c}^2-1\right)T^3, \tag{6.3}$$

$$\lim_{\omega\to 0}\mathcal{F} \equiv 1\,. \tag{6.4}$$

JHEP11(2022)126

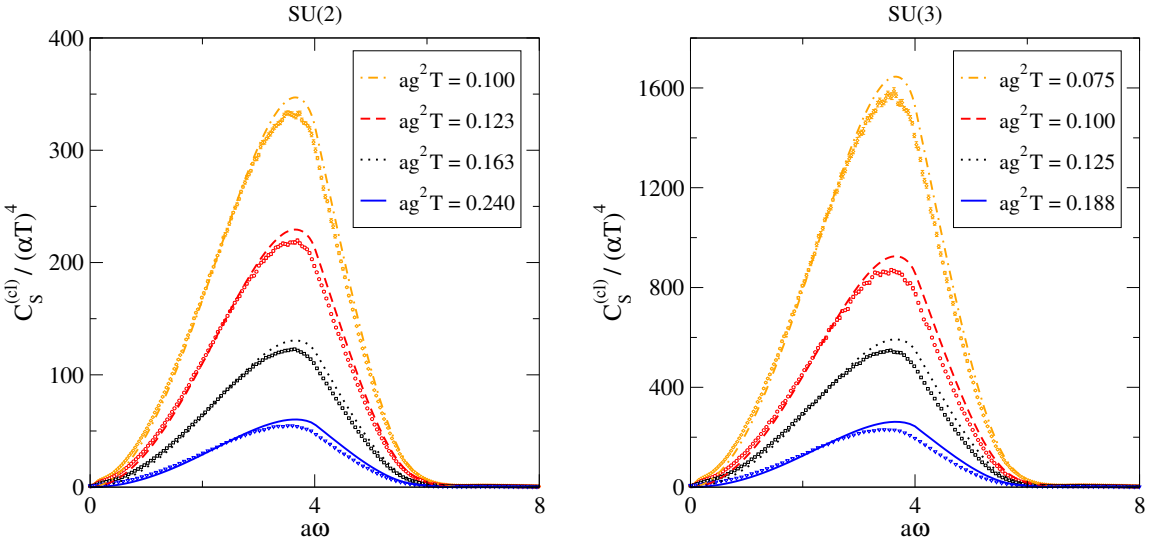

Figure 4. Lattice data (open symbols) for $C_{\rm S}^{(\rm cl)}(\omega)/(\alpha T)^4$, with values of ag^2T chosen from the scaling regime (cf. figure 3), compared with the perturbative contribution from appendix A (lines). The latter is a fairly good approximation in the UV domain $\omega \sim 1/a$, with the small discrepancy conceivably due to next-to-leading order corrections. Our physics conclusions come instead from the IR domain $a\omega = ag^2T \times \omega/(g^2T) \lesssim 1.3$, cf. figure 5, so we need to zoom very close to the origin to extract them.

Here $\rho_{\rm UV}(\omega)$ denotes a perturbative contribution, applicable to large frequencies $|\omega| \gtrsim gT$. The scaling factor $N_{\rm c}^2 - 1$ in $\Upsilon_{\rm IR}$ conforms with ref. [10], and is reproduced by a perturbative computation, cf. eq. (A.21), where it appears as the dimension of the adjoint representation, $d_{\rm A}$. According to eq. (2.6), the corresponding statistical correlator reads

$$\Delta C_{\rm S}(\omega)\Big|_{\rm cont} \overset{|\omega| \ll gT}{\simeq} \underbrace{2T\Upsilon_{\rm IR}}_{\Gamma_{\rm sph}} \mathcal{F}\left(\frac{\omega^2}{\omega_{\rm IR}^2}, \frac{\omega^2}{\omega_{\rm M}^2}, \ldots\right) . \tag{6.5}$$

The parameters ω_i in eq. (6.5) represent frequency scales, the most IR of which is of order

$$\omega_{\rm IR}\big|_{\rm cont} \simeq c_{\rm IR}\, \alpha^2 N_{\rm c}^2 T\,, \tag{6.6}$$

for a suitable coefficient $c_{\rm IR}$. But there are also other frequency scales, for instance the "magnetic" or Linde scale [35], required for exciting non-perturbative glueball-like states,

$$\omega_{\rm M}\big|_{\rm cont} \simeq c_{\rm M}\, \alpha N_{\rm c} T\,, \tag{6.7}$$

where $c_{\rm M}$ is another coefficient of order unity.

Now, we cannot directly convert eq. (6.5) to lattice units, as one combination $\sim \alpha^2 N_{\rm c}^2 T$, closely related to $\omega_{\rm IR}$, will be modified on the lattice into $\sim \alpha^2 N_{\rm c}^2 T^2 a$. It is understood, however, that modulo an unknown logarithmic dependence, this frequency scale is inversely proportional to a Debye mass scale $m_{\rm D}^2$ [24], where

$$m_{\rm D,cont}^2 \overset{N_{\rm f}=0}{=} \frac{N_{\rm c}\, g^2 T^2}{3}\,, \quad m_{\rm D,latt}^2 = 2N_{\rm c}\, g^2 T \times \frac{\Sigma_{v^1}}{4\pi a}\,. \tag{6.8}$$

JHEP11(2022)126

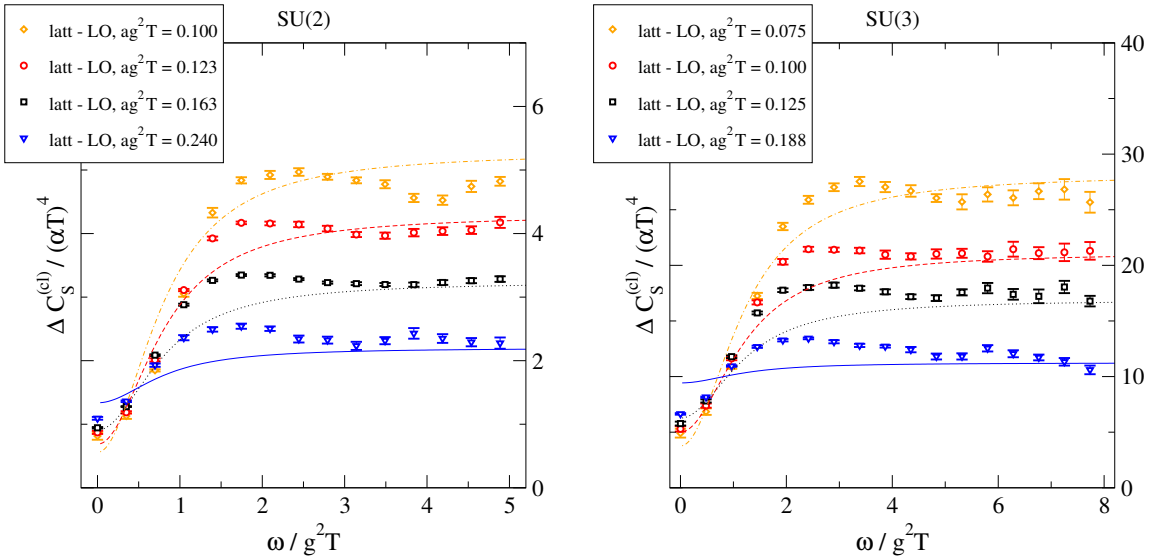

Figure 5. Lattice data for $\Delta C_{\rm S}^{(\rm cl)}(\omega)/(\alpha T)^4$ as a function of $\omega/(g^2T)$, after the subtraction of the perturbative contribution from appendix A, computed up to leading order ("LO"). The lines indicate a qualitative representation of the subtracted data, according to eqs. (6.13) and (6.14).

The coefficient here has the numerical value $\Sigma_{v^1} \approx 2.1498783949$, where we adopted the more general notation of ref. [38]. Therefore, continuum estimates can be converted into lattice estimates, by rescaling them with appropriate powers of the Debye mass squared [24].

Concretely, multiplying the intercept $\Gamma_{\rm sph}$ by $m^2_{\rm D,cont}/m^2_{\rm D,latt}$, we expect the $\omega \to 0$ limit to take the form

$$\lim_{\omega\to 0} \frac{\Delta C_{\rm S}^{(\rm cl)}(\omega)}{(\alpha T)^4}\bigg|_{\rm latt} \simeq \frac{m^2_{\rm D,cont}}{m^2_{\rm D,latt}} \left\{ \lim_{\omega\to 0} \frac{\Delta C_{\rm S}(\omega)}{(\alpha T)^4}\bigg|_{\rm cont} \right\} \simeq \frac{\kappa\, N_{\rm c}^3\, (N_{\rm c}^2-1)\, a g^2 T}{3\Sigma_{v^1}} \,. \tag{6.9}$$

Scaling similarly the width from eq. (6.6), we find

$$\omega_{\rm IR}\big|_{\rm latt} \simeq \frac{m^2_{\rm D,cont}}{m^2_{\rm D,latt}}\, \omega_{\rm IR}\big|_{\rm latt} \simeq \frac{c_{\rm IR}\, a\, (g^2 T N_{\rm c})^2}{24\pi \Sigma_{v^1}} \,. \tag{6.10}$$

In contrast, the magnetic scale $\omega_{\rm M}$ from eq. (6.7) should remain intact on the lattice.

Taking a look at figure 5, we observe that the intercept at $\omega \to 0$ scales towards zero as the lattice spacing is decreased, in accordance with eq. (6.9). But the curves cross each other as ω is increased, and the plateau obtained at $\omega \gtrsim g^2T$ scales in the opposite direction, as $\sim 1/(ag^2T)$. This suggests that

$$\mathcal{F} \overset{\omega \ll \omega_{\rm IR}, \omega_{\rm M}}{\equiv} 1 \,, \qquad \mathcal{F} \overset{\omega \gg \omega_{\rm IR}, \omega_{\rm M}}{\propto} \frac{\omega_{\rm M}^2}{\omega_{\rm IR}^2} \,. \tag{6.11}$$

A simple ansatz satisfying eq. (6.11) reads

$$\mathcal{F} \simeq \frac{1 + \frac{\omega^2}{\omega_{\rm IR}^2}}{1 + \frac{\omega^2}{\omega_{\rm M}^2}} \,, \tag{6.12}$$

JHEP11(2022)126

which gives a 3-parameter model $(\kappa, c_{\rm IR}, c_{\rm M})$ with which to compare the lattice data, viz.

$$\left.\frac{\Delta C_{\rm S}^{(\rm cl)}(\omega)}{(\alpha T)^4}\right|_{\rm latt} \simeq \frac{\kappa\, N_{\rm c}^3(N_{\rm c}^2-1)ag^2T}{3\Sigma_{v^1}}\, \frac{1+\left(\frac{\omega}{g^2T}\right)^2\left(\frac{24\pi\Sigma_{v^1}}{c_{\rm IR}ag^2TN_{\rm c}^2}\right)^2}{1+\left(\frac{\omega}{g^2T}\right)^2\left(\frac{4\pi}{c_{\rm M}N_{\rm c}}\right)^2}\,. \tag{6.13}$$

As demonstrated by the lines in figure 5, the data can indeed be represented with eq. (6.13) on a qualitative level. The representation is not perfect, with perhaps the main deficiency that the threshold between the dip at small ω and the plateau at large ω is somewhat too shallow. Overlooking this feature, the parameters can be chosen as[6]

$$\kappa \simeq 1.5\,, \quad c_{\rm IR} \simeq 106\,, \quad c_{\rm M} \simeq 5.1\,. \tag{6.14}$$

On the qualitative level, the same parameters κ, $c_{\rm IR}$, and $c_{\rm M}$ can be used in the continuum estimates of eqs. (6.4)–(6.7), cf. eq. (7.1).

We conclude this section by recalling that an alternative view on the conversion from lattice to continuum units is that, following refs. [10, 24], we can equate the two Debye masses in eq. (6.8), yielding

$$\frac{g^2}{4\pi} \simeq \frac{ag^2T}{6\Sigma_{v^1}}\,. \tag{6.15}$$

This implies that a study with $ag^2T \simeq 0.20$ can "simulate" a world with $\alpha \simeq 0.015$, as was the case during the reheating period as studied in ref. [14]. The corresponding IR part of the spectral shape could be extracted from figure 5, directly in physical units.

7 Conclusions and outlook

Several frequency scales characterize the dynamics of thermalized non-Abelian fields (cf., e.g., ref. [39]). As reviewed at the end of section 2, the most IR among them, playing an essential role for sphaleron dynamics, is of order $\omega_{\rm IR} \sim (\alpha N_{\rm c} T)^3/m_{\rm E}^2 \sim \alpha^2 N_{\rm c}^2 T/\pi$, where $m_{\rm E}^2 \sim g^2 N_{\rm c} T^2$ is the electric Debye mass squared. A parametrically larger scale is the magnetic one [35], $\omega_{\rm M} \sim \alpha N_{\rm c} T$, which gives the screening masses of spatial correlations in the scalar channel [37]. As such, $\omega_{\rm M}$ determines the magnitude of finite-volume effects [36], but it could also affect real-time phenomena. Further frequency scales originate through $m_{\rm E}$, as well as through the thermal ($\omega_{\rm UV} \sim \pi T$) and confinement ($\omega_{\rm vac} \sim \Lambda_{\overline{\rm MS}}$) scales of the full quantum theory.

The purpose of the present paper has been to carry out numerical simulations within thermally averaged classical SU(2) and SU(3) lattice gauge theories, in order to test which of the frequency scales make an appearance in the IR part of the hot topological charge density spectral function. We have found that this spectral function, or more precisely

[6] Technically, the parameters have been found with a χ^2 minimization of SU(2) data, weighting however the important intercepts at $\omega \to 0$ with an additional factor $\sim 10^3$, but we refrain from citing χ^2 for such a fit, as the representation is a phenomenological one, rather than based on an *a priori* justified ansatz. The SU(3) data was not used for tuning the coefficients, but it is nevertheless represented reasonably well by them.

JHEP11(2022)126

the subtracted statistical correlator $\Delta C_{\rm S}(\omega) \overset{|\omega|\ll T}{\approx} 2T\Delta\rho(\omega)/\omega$, is quadratically growing at $\omega \sim \omega_{\rm IR}$, reaching a plateau at $\omega \sim \omega_{\rm M}$ (cf. figure 5). In terms of eq. (6.4), this means that

$$\Delta\rho(\omega)\big|_{\rm cont} \overset{|\omega|\ll m_{\rm E}}{\simeq} \kappa\,\omega\,\alpha^5 N_{\rm c}^3(N_{\rm c}^2-1)T^3\,\frac{1+\frac{\omega^2}{(c_{\rm IR}\alpha^2 N_{\rm c}^2 T)^2}}{1+\frac{\omega^2}{(c_{\rm M}\alpha N_{\rm c}T)^2}}\,. \tag{7.1}$$

Qualitative values for the coefficients κ, $c_{\rm IR}$ and $c_{\rm M}$ can be found in eq. (6.14). We stress that this representation is of empirical nature, as we are not aware of a solid theoretical argument for the correct frequency shape in the non-perturbative domain.

Further features are expected to appear in $\rho(\omega)$ and $C_{\rm S}(\omega)$ if we go to larger frequencies, $|\omega| \gtrsim m_{\rm E}$. However, in this domain no simulations are needed (if $\alpha N_{\rm c} \ll 1$): the corresponding physics can be addressed with a perturbative computation in the full quantum theory [40]. For $\omega \sim m_{\rm E}$ this requires Hard Thermal Loop resummation, while for $\omega \sim \pi T$ a loop computation suffices. In our study, this physics was addressed by a leading-order perturbative computation within the classical approximation, whose result was subtracted from the lattice measurements. The spectral function in the full quantum theory can then be estimated by adding together the subtracted classical IR and full quantum UV parts [14],

$$\rho(\omega)\big|_{\rm cont} \simeq \Delta\rho(\omega)\big|_{\rm cont} + \rho_{\rm UV}(\omega)\big|_{\rm cont}\,. \tag{7.2}$$

The IR shape that we have found can be rephrased by stating that there is no transport peak in $\Delta C_{\rm S}(\omega)$, but rather a "transport dip", centered at around zero frequency. A physical consequence could be a rapid thermalization of an axion-like inflaton field, as the friction that it feels is not cut off by the width of a transport peak [14], but rather increases if the mass exceeds $\sim \alpha N_{\rm c} T$. In the context of non-perturbative estimates of the sphaleron rate from imaginary-time lattice simulations [6], such a shape represents possibly a challenge, as a fit to the flat part of $\Delta C_{\rm S}(\omega)$ could lead to an overestimate of $\Gamma_{\rm sph}$.

Acknowledgments

Our work was partly supported by the Academy of Finland, under grants 320123, 345070 and 319066, and by the Swiss National Science Foundation (SNSF), under grant 200020B-188712. Simulations were carried out at CSC, the Finnish IT center for Science, making use of the newly released HILA suite [41].

A Perturbative evaluation of the spectral function

The purpose of this appendix is to present a perturbative determination of $C_{\rm S}^{\rm (cl)}(\omega)$, accurate for $\omega \sim 1/a$. A convenient method goes through an unlikely detour, which however has the advantage that we can employ usual perturbative tools, such as Wick contractions and propagators. To this aim, we backtrack to the quantized theory; turn $\mathrm{Tr}\,[(\dots)\,e^{-H/T}]$ into a path integral in a spacetime with an imaginary-time coordinate $\tau \in (0,\beta)$, $\beta \equiv 1/T$; represent the Gauss laws in eq. (3.1) as integrals over an auxiliary field $\tilde{A}_0^a$; and take the classical limit only in the end.[7] The spacetime coordinates are now denoted by $x \equiv (\tau, \mathbf{x})$.

[7] A benefit of this approach is that as an aside we can reproduce the correct leading-order quantum-mechanical result, cf. footnote 8.

JHEP11(2022)126

With discretized spatial directions, the analogue of the continuum field strength, $\tilde{F}^a_{0i}|_{\rm cont} \equiv \partial_0 A^a_i - \mathcal{D}^{ab}_i \tilde{A}^b_0$, can be defined as

$$\tilde{F}_{0i}\,|_{\rm latt} \equiv \frac{1}{iag}[\partial_\tau U_i(x)]U_i^\dagger(x) + \frac{\tilde{A}_0(x) - U_i(x)\tilde{A}_0(x+a\mathbf{i})U_i^\dagger(x)}{a}\,. \tag{A.1}$$

When we represent the Gauss laws as integrals over the Lagrange multiplier $\tilde{A}^a_0$, and turn $e^{-H/T}$ into an imaginary-time path integral, the dependence of the Euclidean action on E_i, incorporating the term from eq. (3.5), takes the form

$$S_{\rm E} \supset \int_0^\beta {\rm d}\tau \sum_{\mathbf{x}} a^3 \sum_i {\rm Tr}\,\Big[\Big(E_i - i\tilde{F}_{0i}\Big)^2 + \tilde{F}^2_{0i}\Big]\,. \tag{A.2}$$

When we subsequently integrate over the Gaussian fields E_i, we see that insertions of the operator E_i get replaced by $i\tilde{F}_{0i}$,

$$\int \mathcal{D}E_i\,(E_i)\,e^{-\#(E_i - i\tilde{F}_{0i})^2} = \int \mathcal{D}E_i\,\Big(\underbrace{E_i - i\tilde{F}_{0i}}_{\rm odd} + i\tilde{F}_{0i}\Big)\,e^{-\#\left(E_i - i\tilde{F}_{0i}\right)^2}\,. \tag{A.3}$$

Therefore, the operator χ from eq. (3.6) is represented as

$$\chi \;\longrightarrow\; \tilde{\chi} \equiv 4ic_\chi\,\epsilon_{ijk}\,g^2\tilde{F}^b_{0i}F^b_{jk}\,. \tag{A.4}$$

Less pedantically, the same recipe could be obtained from a naive Wick rotation of χ from Minkowskian to Euclidean spacetime.

We then compute the imaginary-time correlator corresponding to eq. (2.3),

$$C_{\rm E}(\tau) \equiv \int_{\mathbf{x}} \langle \tilde{\chi}(\tau,\mathbf{x})\,\tilde{\chi}(0,\mathbf{y})\rangle\,, \qquad 0 < \tau < \beta\,. \tag{A.5}$$

After determining the Fourier transform, $C_{\rm E}(\omega_n) \equiv \int_0^\beta {\rm d}\tau\, e^{i\omega_n\tau} C_{\rm E}(\tau)$, where $\omega_n = 2\pi nT$ are Matsubara frequencies, we can extract the retarded correlator, $C_{\rm R}(\omega) = C_{\rm E}(\omega_n \to -i[\omega + i0^+])$. This in turn permits to determine the statistical correlator in accordance with eq. (2.5), $C_{\rm S}(\omega) = [1 + 2n_{\rm B}(\omega)]\,{\rm Im}\,C_{\rm R}(\omega)$. In order to take the classical limit from eq. (2.7), we recall that had we kept $\hbar$ explicit, energy would appear as $\hbar\omega$, so that

$$n_{\rm B}(\hbar\omega) \;\stackrel{\hbar\to 0}{\longrightarrow}\; \frac{T}{\hbar\omega}\,. \tag{A.6}$$

To avoid clutter we suppress $\hbar$ from the notation, and simply adopt eq. (A.6) at the end of the computation (cf. eq. (A.20)).

Proceeding with $C_{\rm E}(\omega_n)$, the electric field $\overline{\mathcal{E}}^{\,b}_i$ is defined in eq. (3.7), and the correspondingly symmetrized Euclidean field strength is denoted by $\tilde{F}^b_{0i}\,|_{\rm symm}$. We associate $T^bF^b_{jk}$ with the clover from eq. (3.8). The links are parametrized as

$$U_j(x) = e^{iag\,T^bA^b_j(x)}\,, \qquad A^b_j(x) = \sum\!\!\!\!\!\!\int_P A^b_j(P)\,e^{iP\cdot\left(x+\frac{a\mathbf{j}}{2}\right)}\,, \tag{A.7}$$

JHEP11(2022)126

where $\oint\!\!\!\!\!\!\sum_P = T\sum_{p_n}\int_{\mathbf{p}}$ represents a Matsubara sum-integral, with $P = (p_n, \mathbf{p})$ and $p_n = 2\pi nT$; and the spatial integral $\int_{\mathbf{p}}$ is restricted to a Brillouin zone. Adopting the notation

$$\tilde{p}_j \equiv \frac{2}{a}\sin\frac{ap_j}{2}\,, \qquad \mathring{p}_j \equiv \frac{1}{a}\sin ap_j\,, \qquad \underset{\sim}{p}_j \equiv \cos\frac{ap_j}{2}\,, \qquad \mathring{p}_j = \tilde{p}_j\,\underset{\sim}{p}_j\,, \tag{A.8}$$

the electric and magnetic fields can be expressed as

$$\tilde{F}^b_{0i}(x)\,|_{\text{symm}} = i\oint\!\!\!\!\!\!\sum_P e^{iP\cdot x}\;\underset{\sim}{p}_i\left[p_n A^b_i(P) - \tilde{p}_i\tilde{A}^b_0(P)\right] + \mathcal{O}(g)\,, \tag{A.9}$$

$$F^b_{jk}(x) = i\oint\!\!\!\!\!\!\sum_P e^{iP\cdot x}\;\left[\mathring{p}_j\,\underset{\sim}{p}_k\,A^b_k(P) - \mathring{p}_k\,\underset{\sim}{p}_j\,A^b_j(P)\right] + \mathcal{O}(g)\,. \tag{A.10}$$

Then the topological charge density from eq. (A.4) becomes

$$\tilde{\chi}(x) = 8ic_\chi\epsilon_{ijk}\,g^2\oint\!\!\!\!\!\!\sum_{P,Q} e^{i(P+Q)\cdot x}\,\underset{\sim}{p}_i\left(\delta_{\mu i}\,p_n - \delta_{\mu 0}\,\tilde{p}_i\right)\,\mathring{q}_k\,\underset{\sim}{q}_j\,A^b_\mu(P)A^b_j(Q) + \mathcal{O}\left(g^3\right)\,, \tag{A.11}$$

where Greek indices take values $\mu \in \{0,1,2,3\}$; Latin indices are spatial, $i,j,k \in \{1,2,3\}$; and repeated indices are summed over.

Carrying out the contractions for eq. (A.5), the Fourier transform takes the form

$$\begin{aligned} C_{\text{E}}(\omega_n) = -64d_{\text{A}}c_\chi^2\,g^4T\sum_{p_n,q_n}\delta_{0,\,\omega_n+p_n+q_n}\int_{\mathbf{p}}\epsilon_{ijk}\epsilon_{suv}\,\underset{\sim}{p}_i\,\underset{\sim}{p}_j\,\mathring{p}_k\,\underset{\sim}{p}_s\,\underset{\sim}{p}_u\,\mathring{p}_v(\delta_{\mu i}\,p_n - \delta_{\mu 0}\,\tilde{p}_i) \\ \times\Big\{\Delta_{\mu\alpha}\,(p_n,\mathbf{p})\;\Delta_{ju}\,(q_n,-\mathbf{p})\;(\delta_{\alpha s}\,p_n - \delta_{\alpha 0}\,\tilde{p}_s) \\ -\Delta_{\mu u}\,(p_n,\mathbf{p})\;\Delta_{j\alpha}\,(q_n,-\mathbf{p})\;(\delta_{\alpha s}\,q_n + \delta_{\alpha 0}\,\tilde{p}_s)\Big\} + \mathcal{O}\left(g^6\right)\,, \end{aligned} \tag{A.12}$$

where $d_{\text{A}} \equiv N_{\text{c}}^2 - 1$, and $\Delta_{\mu\nu}$ is the gauge field propagator.

As a first check, it can be verified that longitudinal parts of the propagators, $\Delta_{\alpha\beta}(P) \supset c\,\tilde{p}_\alpha\tilde{p}_\beta$, where $\tilde{p}_0 \equiv p_n$, yield no contributions. This is fairly simple in the three cases where a "projector", e.g. $\delta_{\alpha s}\,p_n - \delta_{\alpha 0}\,\tilde{p}_s$, is contracted with a propagator, e.g. $\Delta_{\mu\alpha}(P)$. More work, making use of the antisymmetry of the Levi-Civita symbols, is required for the fourth propagator, viz. $\Delta_{ju}(q_n,-\mathbf{p})$, to see that its longitudinal part does not contribute either.

Given that the longitudinal parts do not contribute, propagators can be replaced by their Feynman parts, $\Delta_{\alpha\beta}(P) \to \delta_{\alpha\beta}/(p_n^2 + \tilde{p}^2)$. Here we have introduced the notation

$$\tilde{p}^{2n} \equiv \sum_{j=1}^{3}\tilde{p}_j^{2n}\,, \qquad n = 1,2,\ldots\,. \tag{A.13}$$

We then end up with

$$C_{\text{E}}\,(\omega_n) = -64d_{\text{A}}c_\chi^2\,g^4T\sum_{p_n,q_n}\int_{\mathbf{p}}\delta_{0,\,\omega_n+p_n+q_n}\,\frac{2\,(p_n^2 + p_nq_n)\;\tilde{p}^2\,\Theta\,(\mathbf{p})}{(p_n^2+\tilde{p}^2)\,(q_n^2+\tilde{p}^2)}\,, \tag{A.14}$$

$$\begin{aligned} \Theta\,(\mathbf{p}) = \underset{\sim}{p}_1^2\,\underset{\sim}{p}_2^2\,\underset{\sim}{p}_3^2 &= \left(1 - \frac{a^2\tilde{p}_1^2}{4}\right)\left(1 - \frac{a^2\tilde{p}_2^2}{4}\right)\left(1 - \frac{a^2\tilde{p}_3^2}{4}\right) \\ &= 1 - \frac{a^2\tilde{p}^2}{4} + \frac{a^4\left[\left(\tilde{p}^2\right)^2 - \tilde{p}^4\right]}{32} - \frac{a^6\left[\left(\tilde{p}^2\right)^3 - 3\tilde{p}^2\tilde{p}^4 + 2\tilde{p}^6\right]}{384}\,. \end{aligned} \tag{A.15}$$

Furthermore, by symmetry, we may replace $2\,(p_n^2 + p_nq_n) \to (p_n+q_n)^2 = \omega_n^2$.

JHEP11(2022)126

Subsequently, writing $\delta_{0,\omega_n+p_n+q_n} = T\int_0^\beta \mathrm{d}\tau\, e^{i(\omega_n+p_n+q_n)\tau}$, the two Matsubara sums in eq. (A.14) can be carried out,

$$T\sum_{p_n}\frac{e^{ip_n\tau}}{p_n^2+\tilde{p}^2} = \frac{n_{\rm B}(\tilde{p})}{2\tilde{p}}\Big[e^{\tilde{p}\tau}+e^{\tilde{p}(\beta-\tau)}\Big]\,, \tag{A.16}$$

where $\tilde{p}\equiv\sqrt{\tilde{p}^2}$. When we multiply structures like in eq. (A.16) with each other, cross terms are independent of τ, and yield no contribution in the end. For one of the remaining terms, the Fourier transform yields

$$\int_0^\beta \mathrm{d}\tau\, e^{i\omega_n\tau}\, n_{\rm B}^2\,(\tilde{p})\; e^{2(\beta-\tau)\tilde{p}} = \frac{n_{\rm B}^2\,(\tilde{p})\left(1-e^{2\beta\tilde{p}}\right)}{i\omega_n-2\tilde{p}} = -\frac{1+2n_{\rm B}\,(\tilde{p})}{i\omega_n-2\tilde{p}}\,. \tag{A.17}$$

The cut then gives

$$\mathrm{Im}\left\{\frac{1}{i\omega_n-2\tilde{p}}\bigg|_{\omega_n\to-i[\omega+i0^+]}\right\} = -\pi\delta(\omega-2\tilde{p})\,. \tag{A.18}$$

All in all, this implies that

$$T\sum_{p_n,q_n}\frac{\delta_{0,\omega_n+p_n+q_n}}{(p_n^2+\tilde{p}^2)\,(q_n^2+\tilde{p}^2)} \xrightarrow{\text{cut}} \frac{\pi\left[\delta\,(\omega-2\tilde{p})+\delta\,(\omega+2\tilde{p})\right]\left[1+2n_{\rm B}\,(\tilde{p})\right]}{4\tilde{p}^2}\,. \tag{A.19}$$

The final step is to consider the classical limit from eq. (2.7).[8] Two Bose distributions appear, one from $C_{\rm S}(\omega) = [1+2n_{\rm B}(\omega)]\,\rho(\omega)$, cf. eq. (2.5), and the other from eq. (A.19). Reinstituting $\hbar$, we are faced with

$$\lim_{\hbar\to0}\left[1+2n_{\rm B}\,(\hbar\omega)\right]\left[1+2n_{\rm B}\left(\frac{\hbar\omega}{2}\right)\right] = \frac{2T}{\hbar\omega}\frac{4T}{\hbar\omega}\,. \tag{A.20}$$

Then, from eqs. (A.14), (A.15) and (A.19),

$$C_{\rm S}^{\rm (cl)}(\omega) = 64 d_{\rm A} c_\chi^2\, g^4 T^2 \int_{\mathbf{p}} \pi\delta\left(\tilde{p}-\frac{\omega}{2}\right)\Theta(\mathbf{p})\,. \tag{A.21}$$

Proceeding to the numerical evaluation, we employ dimensionless units, writing

$$p_i \equiv \frac{q_i}{a}\,, \qquad \tilde{p}_i \equiv \frac{\tilde{q}_i}{a}\,. \tag{A.22}$$

Normalizing like in eq. (3.12), eq. (A.21) becomes

$$\frac{C_{\rm S}^{\rm (cl)}(\omega)}{(\alpha T)^4} \overset{ag^2T\ll a\omega}{\approx} \frac{4d_{\rm A}}{(ag^2T)^2}\,\mathcal{C}\left(\frac{a\omega}{2}\right)\,, \tag{A.23}$$

[8] If we take no classical limit but go to continuum, where $\tilde{p}\to p$ and $a\to 0$, then eqs. (A.14)–(A.19) reproduce an expression employed in ref. [14],

$$\mathrm{Im}\, C_{\rm E}(\omega_n\to-i[\omega+i0^+]) = 64 d_{\rm A} c_\chi^2\, g^4 \int_{\mathbf{p}} p^2[1+2n_{\rm B}(p)]\pi\delta(\omega-2p) = \frac{d_{\rm A} c_\chi^2\, g^4\omega^4}{\pi}\left[1+2\,n_{\rm B}\Big(\frac{\omega}{2}\Big)\right].$$

JHEP11(2022)126

where the frequency range is the one in which corrections from higher loop orders are small. The function $\mathcal{C}$ has been defined as

$$\begin{aligned}\mathcal{C}(x) &\equiv \int_0^\pi \frac{\mathrm{d}^3\mathbf{q}}{\pi^2}\,\delta\left(\tilde{q}-x\right)\,\Theta\left(\frac{\mathbf{q}}{a}\right)\\ &= \frac{2}{\pi^2}\int_0^\pi \mathrm{d}q_1\int_0^{q_1}\mathrm{d}q_2\int_0^\pi \mathrm{d}q_3\,\delta(\tilde{q}-x)\,\Theta\left(\frac{q_1}{a},\frac{q_2}{a},\frac{q_3}{a}\right)\,. \end{aligned} \tag{A.24}$$

Here we made use of the symmetry of Θ in $p_1 \leftrightarrow p_2$. The last step is to carry out the integral over q_3, which yields [here ϕ is an arbitrary function, $\phi(q_3) = \Theta(\frac{q_1}{a},\frac{q_2}{a},\frac{q_3}{a})$]

$$\begin{aligned}\int_0^\pi \mathrm{d}q_3\,\delta(\tilde{q}-x)\,\phi(q_3) = \theta\left(\frac{x^2}{4}-\sin^2\frac{q_1}{2}-\sin^2\frac{q_2}{2}\right)\theta\left(1+\sin^2\frac{q_1}{2}+\sin^2\frac{q_2}{2}-\frac{x^2}{4}\right)\\ \times\frac{x}{|\sin(q_3)|}\,\phi\left(2\arcsin\sqrt{\frac{x^2}{4}-\sin^2\frac{q_1}{2}-\sin^2\frac{q_2}{2}}\right)\,,\end{aligned} \tag{A.25}$$

where θ is the Heaviside function.[9] The argument of ϕ permits for us to evaluate $x/|\sin(q_3)|$ as well as powers like $\tilde{q}^{2n}$. Numerical illustrations can be found as curves in figure 4.

References

[1] G. 't Hooft, *Computation of the quantum effects due to a four-dimensional pseudoparticle*, *Phys. Rev. D* **14** (1976) 3432 [*Erratum ibid.* **18** (1978) 2199] [INSPIRE].

[2] V.A. Kuzmin, V.A. Rubakov and M.E. Shaposhnikov, *On the anomalous electroweak baryon-number nonconservation in the early universe*, *Phys. Lett. B* **155** (1985) 36 [INSPIRE].

[3] M. D'Onofrio, K. Rummukainen and A. Tranberg, *Sphaleron Rate in the Minimal Standard Model*, *Phys. Rev. Lett.* **113** (2014) 141602 [arXiv:1404.3565] [INSPIRE].

[4] F.R. Klinkhamer and N.S. Manton, *A saddle-point solution in the Weinberg-Salam theory*, *Phys. Rev. D* **30** (1984) 2212 [INSPIRE].

[5] L.D. McLerran, E. Mottola and M.E. Shaposhnikov, *Sphalerons and axion dynamics in high-temperature QCD*, *Phys. Rev. D* **43** (1991) 2027 [INSPIRE].

[6] L. Altenkort, A.M. Eller, O. Kaczmarek, L. Mazur, G.D. Moore and H.-T. Shu, *Sphaleron rate from Euclidean lattice correlators: An exploration*, *Phys. Rev. D* **103** (2021) 114513 [arXiv:2012.08279] [INSPIRE].

[7] K. Freese, J.A. Frieman and A.V. Olinto, *Natural inflation with pseudo Nambu-Goldstone bosons*, *Phys. Rev. Lett.* **65** (1990) 3233 [INSPIRE].

[8] M.M. Anber and L. Sorbo, *Naturally inflating on steep potentials through electromagnetic dissipation*, *Phys. Rev. D* **81** (2010) 043534 [arXiv:0908.4089] [INSPIRE].

[9] The integration boundaries for q_1 and q_2 are modified by the two Heaviside functions.

JHEP11(2022)126

[9] E. Pajer and M. Peloso, *A review of Axion Inflation in the era of Planck*, *Class. Quant. Grav.* **30** (2013) 214002 [arXiv:1305.3557] [INSPIRE].

[10] G.D. Moore and M. Tassler, *The sphaleron rate in* SU(N) *gauge theory*, *JHEP* **02** (2011) 105 [arXiv:1011.1167] [INSPIRE].

[11] K.V. Berghaus, P.W. Graham and D.E. Kaplan, *Minimal warm inflation*, *JCAP* **03** (2020) 034 [arXiv:1910.07525] [INSPIRE].

[12] S. Das, G. Goswami and C. Krishnan, *Swampland, axions, and minimal warm inflation*, *Phys. Rev. D* **101** (2020) 103529 [arXiv:1911.00323] [INSPIRE].

[13] Y. Reyimuaji and X. Zhang, *Warm-assisted natural inflation*, *JCAP* **04** (2021) 077 [arXiv:2012.07329] [INSPIRE].

[14] M. Laine and S. Procacci, *Minimal warm inflation with complete medium response*, *JCAP* **06** (2021) 031 [arXiv:2102.09913] [INSPIRE].

[15] F. Takahashi and W. Yin, *Challenges for heavy QCD axion inflation*, *JCAP* **10** (2021) 057 [arXiv:2105.10493] [INSPIRE].

[16] V. Kamali, H. Moshafi and S. Ebrahimi, *Minimal warm inflation and TCC*, arXiv:2111.11436 [INSPIRE].

[17] M. Mirbabayi and A. Gruzinov, *Shapes of non-Gaussianity in warm inflation*, arXiv:2205.13227 [INSPIRE].

[18] P. Klose, M. Laine and S. Procacci, *Gravitational wave background from non-Abelian reheating after axion-like inflation*, *JCAP* **05** (2022) 021 [arXiv:2201.02317] [INSPIRE].

[19] D.T. Son and A.O. Starinets, *Minkowski-space correlators in AdS/CFT correspondence: recipe and applications*, *JHEP* **09** (2002) 042 [hep-th/0205051] [INSPIRE].

[20] D. Bödeker, L.D. McLerran and A.V. Smilga, *Really computing nonperturbative real time correlation functions*, *Phys. Rev. D* **52** (1995) 4675 [hep-th/9504123] [INSPIRE].

[21] D.Y. Grigoriev, V.A. Rubakov and M.E. Shaposhnikov, *Topological transitions at finite temperatures: a real time numerical approach,*, *Nucl. Phys. B* **326** (1989) 737 [INSPIRE].

[22] J. Ambjørn, T. Askgaard, H. Porter and M.E. Shaposhnikov, *Sphaleron transitions and baryon asymmetry: A numerical, real-time analysis*, *Nucl. Phys. B* **353** (1991) 346 [INSPIRE].

[23] D. Bödeker, *Classical real time correlation functions and quantum corrections at finite temperature*, *Nucl. Phys. B* **486** (1997) 500 [hep-th/9609170] [INSPIRE].

[24] P.B. Arnold, *Hot B violation, the lattice, and hard thermal loops*, *Phys. Rev. D* **55** (1997) 7781 [hep-ph/9701393] [INSPIRE].

[25] G.D. Moore and K. Rummukainen, *Classical sphaleron rate on fine lattices*, *Phys. Rev. D* **61** (2000) 105008 [hep-ph/9906259] [INSPIRE].

[26] D. Bödeker, *On the effective dynamics of soft non-Abelian gauge fields at finite temperature*, *Phys. Lett. B* **426** (1998) 351 [hep-ph/9801430] [INSPIRE].

[27] D. Bödeker, *A local Langevin equation for slow long-distance modes of hot non-Abelian gauge fields*, *Phys. Lett. B* **516** (2001) 175 [hep-ph/0012304] [INSPIRE].

[28] P.B. Arnold, D.T. Son and L.G. Yaffe, *Effective dynamics of hot, soft non-Abelian gauge fields: Color conductivity and* $\log(1/\alpha)$ *effects*, *Phys. Rev. D* **59** (1999) 105020 [hep-ph/9810216] [INSPIRE].

JHEP11(2022)126

[29] G.D. Moore, *The Sphaleron rate: Bödeker's leading log*, *Nucl. Phys. B* **568** (2000) 367 [hep-ph/9810313] [INSPIRE].

[30] P.B. Arnold and L.G. Yaffe, *High temperature color conductivity at next-to-leading log order*, *Phys. Rev. D* **62** (2000) 125014 [hep-ph/9912306] [INSPIRE].

[31] J.B. Kogut and L. Susskind, *Hamiltonian formulation of Wilson's lattice gauge theories*, *Phys. Rev. D* **11** (1975) 395 [INSPIRE].

[32] M. Lüscher, *Construction of a selfadjoint, strictly positive transfer matrix for Euclidean lattice gauge theories*, *Commun. Math. Phys.* **54** (1977) 283 [INSPIRE].

[33] P. Di Vecchia, K. Fabricius, G.C. Rossi and G. Veneziano, *Preliminary evidence for* $U_A(1)$ *breaking in QCD from lattice calculations*, *Nucl. Phys. B* **192** (1981) 392 [INSPIRE].

[34] G.D. Moore, *Motion of Chern-Simons number at high temperatures under a chemical potential*, *Nucl. Phys. B* **480** (1996) 657 [hep-ph/9603384] [INSPIRE].

[35] A.D. Linde, *Infrared problem in thermodynamics of the Yang-Mills gas*, *Phys. Lett. B* **96** (1980) 289 [INSPIRE].

[36] H.B. Meyer, *Finite volume effects in thermal field theory*, *JHEP* **07** (2009) 059 [arXiv:0905.1663] [INSPIRE].

[37] P.B. Arnold and L.G. Yaffe, *Non-Abelian Debye screening length beyond leading order*, *Phys. Rev. D* **52** (1995) 7208 [hep-ph/9508280] [INSPIRE].

[38] M. Laine, G.D. Moore, O. Philipsen and M. Tassler, *Heavy quark thermalization in classical lattice gauge theory: lessons for strongly-coupled QCD*, *JHEP* **05** (2009) 014 [arXiv:0902.2856] [INSPIRE].

[39] P.B. Arnold and L.G. Yaffe, *Effective theories for real time correlations in hot plasmas*, *Phys. Rev. D* **57** (1998) 1178 [hep-ph/9709449] [INSPIRE].

[40] M. Laine, A. Vuorinen and Y. Zhu, *Next-to-leading order thermal spectral functions in the perturbative domain*, *JHEP* **09** (2011) 084 [arXiv:1108.1259] [INSPIRE].

[41] *HILA lattice simulation framework*, https://github.com/CFT-HY/HILA.

JHEP11(2022)126